(Preprint) AAS-22-117

A ROBUST IMAGE PROCESSING PIPELINE FOR PLANETS LINE-OF-SIGHT EXTRACTION FOR DEEP-SPACE AUTONOMOUS CUBESATS NAVIGATION

E. Andreis[*], P. Panicucci[†], V. Franzese[‡], and F. Topputo[§]

The adoption of CubeSats marks the beginning of new momentum in interplanetary exploration, owing to their low cost as compared to standard missions. Yet, the proliferation of deep-space CubeSats will cause the saturation of the ground networks, hindering the traditional navigation through ground-based radiometric tracking. The solution to this issue resides in the exploitation of autonomous miniaturized probes.

Autonomous vision-based navigation (VBN) and robust Image Processing (IP) are crucial to overcome these limitations. This is because of the capability of such algorithms to provide near real-time information to navigation filters on-board. For these reasons the use of passive cameras, in combination with IP algorithms, provides compelling navigation performances with light and cost-effective hardware. It is thus necessary to develop efficient, robust, and fast IP algorithms that must be strongly integrated within navigation filters. In the context of deep space navigation, CubeSats can perform celestial triangulation by exploiting visible planets as beacons. Given these considerations, this paper proposes an innovative and robust planets line-of-sight extraction procedure applicable to interplanetary autonomous CubeSats. In particular, the work focuses on the description of a new methodology adopted for star pattern and planets identification. Statistical results show that a 3σ accuracy of 30 arcsec is obtained for the planet line-of-sight (LoS) extraction with a failure lower than 1% when the spacecraft position is known with a 3σ accuracy of 10^5 km.

INTRODUCTION

The adoption of autonomous CubeSats marks the beginning of a new era in deep-space exploration.[1] Thanks to the cutting down on the production costs, nanosats grant the democratization of interplanetary exploration and exploitation, opening access to space also to small companies and universities. Nevertheless, the CubeSats flourishing proliferation could be obstructed by the saturation of ground control slots.[2] To prevent this, self-driving deep-space CubeSats, which do not require any ground-based support, would overcome these limitations.[3] The ability to autonomously navigate and move in the Solar System requires the Guidance, Navigation, and Control (GNC) to be

[*]PhD Candidate, Department of Aerospace Science and Technology, Politecnico di Milano, Milano, Italy.
[†]Postdoctoral Research Fellow, Department of Aerospace Science and Technology, Politecnico di Milano, Milano, Italy.
[‡]Postdoctoral Research Fellow, Department of Aerospace Science and Technology, Politecnico di Milano, Milano, Italy.
[§]Full Professor, Department of Aerospace Science and Technology, Politecnico di Milano, Milano, Italy.

autonomous. From a navigation perspective, the spacecraft must be aware of the external environment by determining its position with respect to the Solar System reference frame without ground support. For this purpose, planet positions observed during the cruise can be exploited to triangulate the spacecraft position.[4] In this context, one of the most relevant issues concerns the recognition and labeling of the planet in the image against the stellar background.
This work, framed within the ERC-funded EXTREMA (Engineering Extremely Rare Events in Astrodynamics for Deep-Space Mission in Autonomy) project,[5] aims to prove that the autonomous planets line-of-sight extraction from images is possible during deep-space cruise without ground support to pave the way to autonomous navigation.
The paper is structured as follows. First, the "Projective Geometry Preliminaries" section defines the work-frame adopted in this work. Then, the "Methodology" section describes the step-by-step procedure followed by the IP pipeline for the extraction of the planet LoS direction. Finally, the "Simulation" section presents the performances of the procedure in different scenarios and discusses the robustness of the algorithm.

NOTATION

In this paper the following notation is used:

- 3D vectors are denoted with lower case bold text, such as $\boldsymbol{r}$, and 2D vectors are denoted with upper case bold, such as $\boldsymbol{R}$.
- Matrices are in plain text in brackets, such as $[A]$
- $\mathcal{A} = \{a,\, \boldsymbol{a}_1,\, \boldsymbol{a}_2,\, \boldsymbol{a}_3\}$ is the reference frame centered in a with axes $\boldsymbol{a}_1$, $\boldsymbol{a}_2$, and $\boldsymbol{a}_3$. All the reference frame are right-handed.
- $\mathbb{A} = \{A,\, \boldsymbol{A}_1,\, \boldsymbol{A}_2\}$ is the a 2D reference frame. This reference frame is centered in A with axes $\boldsymbol{A}_1$ and $\boldsymbol{A}_2$ which are orthonormal.
- All rotation have a passive function. This means that points, vectors and all geometrical entities are fixed in space and the reference frame is translated and rotated.
- The rotation matrix from $\mathcal{S}$ to $\mathcal{C}$ is $[CS]$
- The vector $\boldsymbol{r}$ expressed in the $\mathcal{S}$ reference frame is denoted ${}^{\mathcal{S}}\boldsymbol{r}$
- The 3D vector $\boldsymbol{r}$ in its homogeneous form is labeled ${}_h\boldsymbol{r}$ and the 2D vector $\boldsymbol{R}$ in its homogeneous form is labeled ${}_h\boldsymbol{R}$
- The projection of the 3D vector $\boldsymbol{r}$ on the 2D image is labeled $\boldsymbol{R}$
- The identity matrix of dimension n is labeled $[\mathbb{I}_n]$
- The zero $n \times m$ matrix is labeled $[\mathbb{0}_{n\times m}]$
- The skew symmetric matrix associated with the cross product $\boldsymbol{x} \times \boldsymbol{y}$ is $[\boldsymbol{x}^\wedge]$. Thus $\boldsymbol{x} \times \boldsymbol{y} = [\boldsymbol{x}^\wedge]\, \boldsymbol{y} = -\,[\boldsymbol{y}^\wedge]\, \boldsymbol{x}$

PROJECTIVE GEOMETRY PRELIMINARIES

Let ${}^{\mathcal{N}}\boldsymbol{r}_{\rm pl}$ and ${}^{\mathcal{N}}_{h}\boldsymbol{r}_{\rm pl}$ be the planet position vector in the inertial reference frame $\mathcal{N} = \{n, \boldsymbol{n}_1, \boldsymbol{n}_2, \boldsymbol{n}_3\}$ expressed with non-homogeneous and homogeneous coordinates, respectively, and let ${}^{\mathcal{N}}\boldsymbol{r}$ be the spacecraft position in non-homogeneous coordinates.
The position of the planet as seen by the spacecraft in $\mathcal{N}$ is described as

$$ {}^{\mathcal{N}}\boldsymbol{\rho} = {}^{\mathcal{N}}\boldsymbol{r}_{\rm pl} - {}^{\mathcal{N}}\boldsymbol{r} \tag{1} $$

Let a projective camera observe the planet. The camera frame is defined as $\mathcal{C} = \{c, \boldsymbol{c}_1, \boldsymbol{c}_2, \boldsymbol{c}_3\}$. The vector ${}^{\mathcal{N}}\boldsymbol{\rho}$ can be transformed in $\mathcal{C}$ though a passive rotation from $\mathcal{N}$ to $\mathcal{C}$ and applied by the attitude matrix $[CN]$:

$$ {}^{\mathcal{C}}\boldsymbol{\rho} = [CN]\,{}^{\mathcal{N}}\boldsymbol{\rho} \tag{2} $$

For the definition of the attitude matrix, in this work, the Axis-Azimuth representation[6] is adopted. By assuming that the camera boresight is coincident with the spacecraft-fixed reference frame third axis, $[CN]$ is

$$ [CN] = [R_3(\alpha)]\,[R_2(\pi/2 - \delta)]\,[R_3(\phi)] \tag{3} $$

where $[CN]$ is obtained through a succession of counterclockwise rotations taking into account the camera pointing angles: right ascension $\alpha \in [0°, 360°]$, declination $\delta \in [-90°, 90°]$, and twist angle $\phi \in [0°, 360°]$.
Once the position of the planet as seen by the spacecraft in $\mathcal{C}$ is computed (see Eq. 2), the 3D point is projected on the image plane exploiting the pin-hole camera model. The $2D$ projection ${}^{\mathbb{C}}\boldsymbol{R} = [{}^{\mathbb{C}}X_{\rm pl}, {}^{\mathbb{C}}Y_{\rm pl}]^{\top}$ is so obtained, where $\mathbb{C} = \{C, \boldsymbol{C}_1, \boldsymbol{C}_2\}$ represents the $2D$ digital camera frame: $\boldsymbol{C}_1$ points to the right, $\boldsymbol{C}_2$ downward, and the center C is placed at the upper left-hand corner of the image. At this point, since the central projection is expressed in a linear fashion in homogeneous coordinates,[7] the following relationships exploit this formalism. The transformation of the planet position vectors in homogeneous coordinates from $\mathcal{N}$ to $\mathbb{C}$ is compactly described as

$$ {}^{\mathbb{C}}_{h}\boldsymbol{R}_{\rm pl} = [K]\,\underbrace{[CN]\Big[[\mathbb{I}_3]\big| - {}^{\mathcal{N}}\boldsymbol{r}\Big]}_{{}^{\mathcal{C}}\boldsymbol{\rho}}\,{}^{\mathcal{N}}_{h}\boldsymbol{r}_{\rm pl} \tag{4} $$

where $[K]$ is the intrinsic camera matrix.[7]
Finally, the planet position projection in $\mathbb{C}$ in non-homogeneous coordinates becomes

$$ {}^{\mathbb{C}}\boldsymbol{R}_{\rm pl} = \begin{pmatrix} {}^{\mathbb{C}}R_{\rm pl_1} \\ {}^{\mathbb{C}}R_{\rm pl_2} \end{pmatrix} = \begin{pmatrix} \frac{{}^{\mathbb{C}}_{h}R_{\rm pl_1}}{{}^{\mathbb{C}}_{h}R_{\rm pl_3}} \\ \frac{{}^{\mathbb{C}}_{h}R_{\rm pl_2}}{{}^{\mathbb{C}}_{h}R_{\rm pl_3}} \end{pmatrix} \tag{5} $$

where $R_{\rm pl_i}$ is the ith component of the planet position projection in $\mathbb{C}$ in homogeneous coordinates. Through an analogous procedure, stars are projected on the camera frame. Stars positions are usually stored in catalogs, such as the Hipparcos catalogue,[8] which provides their right ascension and declination on the celestial sphere.[9]
It is important to note that the geometrical relationship outlined in this section are useful not only for image rendering but also for IP and VBN algorithms.

METHODOLOGY

In this section, the developed IP pipeline is expounded. The final goal of the algorithm is the extraction of the planet LoS direction, which has been shown to be a valuable observable for deep space VBN even with limited-performance cameras.[10,11] To do so, the IP algorithm performs two steps sequentially:

1. The identification of the star-pattern and the determination of the spacecraft attitude: Firstly, a search-less method based on the k-vector technique[12,13] and bulked up with a RANSAC[14] procedure is adopted, which also allow the recognition of non-stellar objects (spikes), such as planets and uncatalogued stars, in the image. Then, by knowing the stars identifiers, it is thus possible to extract their relative inertial position vectors from the onboard stars catalog and compute the probe orientation.

2. The recognition of the planets in the image and the extraction of their LoS directions: Firstly, the expected planet position projection and its relative uncertainty ellipse are computed. Then, if one or more spikes are contained in the uncertainty ellipse, the spike closest to the expected planet position projection is identified as the position projection of the planet itself, and its LoS direction is extracted from the image.

The flowchart of the image processing pipeline is shown in Figure 1.

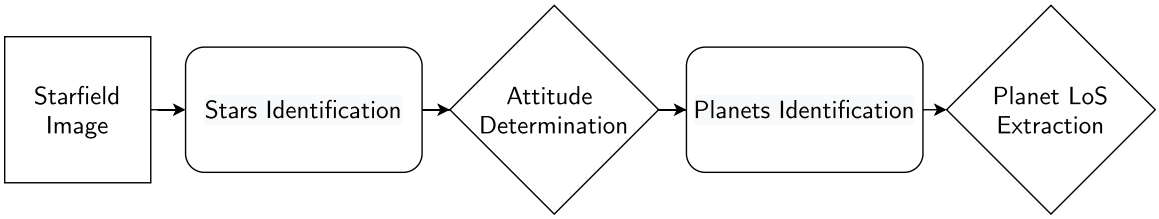

Figure 1: Image Processing WorkFlow

Stars Identification and Attitude Determination Procedure

To determine the probe attitude, the stars-pattern has to be first identified. To do this, three steps shall be performed: 1) the centroids of the bright objects in the image have to be determined, 2) the bright objects have to be recognized as stars and matched with the corresponding values in the onboard catalog, and 3) the RANSAC algorithm has to be applied to increase the robustness of the stars-matching step.

Centroids Computation To compute the centroids of the bright objects in the image, the procedure presented in Reference 9 is applied. First, a threshold value K, expressed in pixel intensity, is set up to remove the background noise. In this work, a dynamic thresholding method is exploited, in which K is a function of the image intensity.[15,16] That is,

$$\begin{cases} K = \mu + k\,\sigma \\ \mu = \frac{1}{N}\sum_{i,j} I_{i,j} \\ \sigma = \sqrt{\frac{1}{N}\sum_{i,j} |I_{i,j} - \mu|^2} \end{cases} \tag{6}$$

where N is the total number of the pixels, $I_{i,j}$ the intensity of the pixel with pixel coordinates (i, j), μ the intensity mean, σ the intensity standard deviation over the image, and k the tuning parameter. Second, the coordinates of the brightest pixels in the image and its associated squared centroiding window or Region-Of-Interest (ROI), which delimits each brightest pixel with a margin of one pixel on each side, are identified. Third, the object centroid is found by computing the image momenta:[17]

$$\begin{cases} I_{00} = \sum_{i,j} I_{i,j}\ w_{i,j} \\ I_{10} = \sum_{i,j} x_i\ I_{i,j}\ w_{i,j} \\ I_{01} = \sum_{i,j} y_j\ I_{i,j}\ w_{i,j} \end{cases} \tag{7}$$

where i and j are the pixels within the ROI, x and y the pixel coordinates, I_{10} and I_{01} the momenta of the ROI in the two directions, I_{00} the overall intensity within the ROI, and $w_{i,j}$ a weighting parameter associated with the pixel at coordinates (i, j). In this work, the weighting parameter is defined as $w_{i,j} = I_{i,j}$ to give more importance to brighter pixels inside the ROI. Finally, the sub-pixel centroid coordinates are computed as:

$$x_c = \frac{I_{10}}{I_{00}} \qquad\qquad y_c = \frac{I_{01}}{I_{00}} \tag{8}$$

This process is repeated for all the brightest pixels in the image.

Stars Matching Once the centroids of the brightest pixels are found, the core of the stars identification procedure starts. The goal of the star identification procedure is to recognize, among the found centroids, the ones which are stars projection in the image. To do so, the problem is rewritten as a registration problem whose goal is to find the correct correspondence between the observed stars' indices and the cataloged stars' indices.[18] For this purpose, a search-less algorithm is adopted. This particular star identification procedure is selected for three main reasons:[19] 1) It is fast since it does not require a searching-phase, 2) It can be exploited in the Lost-In-Space (LIS) phase since it does not need an a-priori attitude guess, and 3) It allows to identify the non-stellar objects (spikes), whose utility will be seen later on.

The search-less algorithm relies on the matching of a ground-computed on-board-stored catalog of stars' invariants with the same invariant as computed from the measured stars in the image. In this work, the algorithm exploits as invariant only the inter-star angle, i.e., the angle between two unit stars vectors, whereas no magnitude information is considered. Since this procedure is well known in the literature, only the general workflow is illustrated, whereas further details can be found in Reference 12 and 18.

Firstly, starting from the i_{obs}th bright ROI centroid, all the interstar angles between i_{obs}th and the other ROI centroids j_{obs} in the image are evaluated. At each measured interstar angle θ_{obs} corresponds more catalogued interstar angles, each one relative to a catalogued stars-pair $(i_c - j_c)$. Indeed, all the catalogued star-pairs whose interstar angle falls inside the range $[\cos(\theta_{\text{obs}} + 2\epsilon), \cos(\theta_{\text{obs}} - 2\epsilon)]$, where ϵ is the optical instrument precision, are considered as candidate matches. The stars i_c and j_c associated to these star-pairs are regrouped in two vectors $\boldsymbol{I}_c$ and $\boldsymbol{J}_c$. If the occurrence of the two most frequent identifiers in $\boldsymbol{I}_c$ and $\boldsymbol{J}_c$ respect a certain threshold value, the most frequent identifier in $\boldsymbol{I}_c \cup \boldsymbol{J}_c$ is selected as the reference star and associate to i_{obs}. At this point, the other object j_{obs} is identified by looking for the star identifier coupled to the reference star among the candidate star-pairs.

When the ratio between the number of objects and the number of spikes is low, the star pattern can be not identified by the algorithm. In this case, the tuning value k of K (see Eq. 6), which is

needed for the removal of the background noise, is increased and the star identification procedure is repeated. This results in the diminishing of the number of bright objects in the image, which can ultimately lead to the removal of some spikes. This procedure is repeated until the pattern of the stars is recognized or less than three stars are detected. Figure 2 shows the results obtained after the first (Figure 2a) and the second (Figure 2b) iteration of the star identification procedure, in which the value of k goes from 10 to 12, respectively. It can be noticed that the number of bright objects detected by the centroids computation procedure in Figure 2b is minor than the one in Figure 2a.

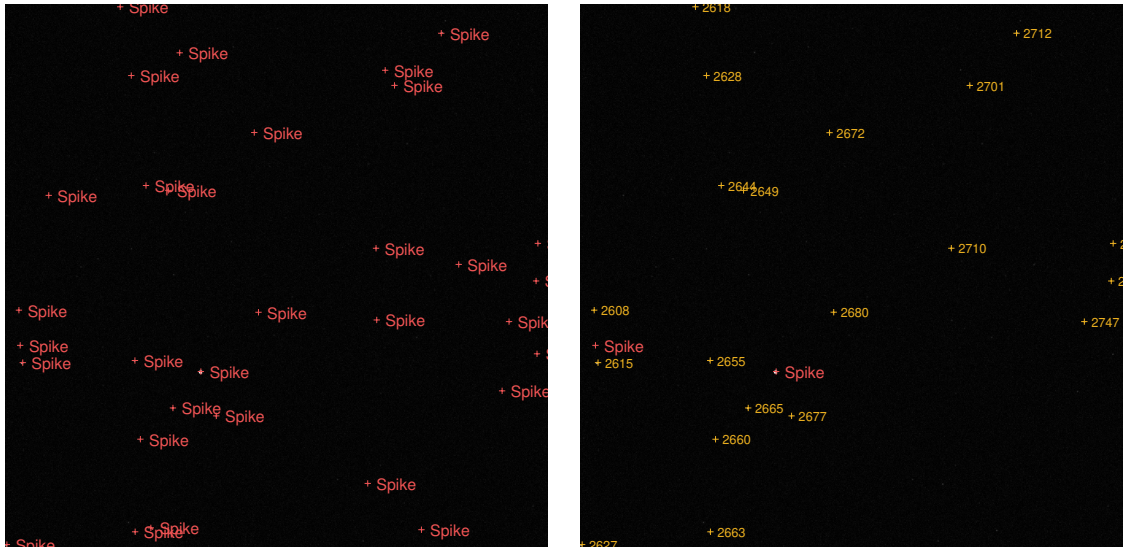

(a) Stars pattern not recognized

(b) Star pattern recognized

Figure 2: Results before and after having increased the tuning parameter k

When the pattern of the stars is recognized, the stars identification algorithm gives as output the vector $\boldsymbol{s}_{\mathrm{indx}} = [s_{\mathrm{indx}_1}, ..., s_{\mathrm{indx}_n}]^\top$ and the matrix $[{}^{\mathcal{N}}s] = [{}^{\mathcal{N}}\boldsymbol{s}_1, ..., {}^{\mathcal{N}}\boldsymbol{s}_n]$, which contain the stars identifiers and the associated stars position in the $\mathcal{N}$ reference frame, respectively. Moreover, also a vector including the position of the spikes is delivered.

RANSAC Algorithm To increase the robustness of the algorithm and lower the possibility of a wrong stars identification, a RANdom SAmple Consensus (RANSAC) procedure is included in the IP pipeline. The RANSAC algorithm of Fischler and Bolls[20] is a general and robust iterative method able to estimate parameters of a mathematical model from a set of input data with a large proportion of outliers.[14] It can be also seen as an outliers detection method.
In this work, the RANSAC algorithm is applied to detect the misidentified stars (outliers) by exploiting the attitude of the spacecraft as the model for the data fitting.
At this aim, n_R samples are considered. For each sample, a subset of 3 stars is randomly selected within the vector $\boldsymbol{s}_{\mathrm{indx}}$ (from now on called $\boldsymbol{s}_{\mathrm{indx}_{\mathrm{old}}}$), and its related spacecraft rotation principal axis $\boldsymbol{e}_i$ is defined. The rotation principal axis $\boldsymbol{e}$ is the model instantiated for the RANSAC procedure. At each $\boldsymbol{e}_i$ is assigned a score dependent on the number of vectors $\boldsymbol{e}_j$ (with $j \neq i$) that are within a distance threshold t of $\boldsymbol{e}_i$. The set of vectors that satisfy this requirement is called the consensus set of $\boldsymbol{e}_i$. The vector $\boldsymbol{e}_i$ that is associated with the largest consensus set is selected as the best model. The size of the consensus set associated with $\boldsymbol{e}_i$ can be determined as the score of $\boldsymbol{e}_i$. The model is then re-estimated using the data in the consensus set: $\boldsymbol{s}_{\mathrm{indx}_{\mathrm{new}}}$ and $[{}^{\mathcal{N}}s_{\mathrm{new}}]$ are

obtained by using all and only the star subsets that generate the vectors contained in the consensus set of the selected model. The remaining stars (outliers) are identified as spikes. If two or more consensus sets are characterized by the same dimension, the best vector is chosen arbitrarily among the vectors $\boldsymbol{e}_i$ related to these consensus sets. Let us look at Figure 3 for a graphical representation of the selection procedure. To the orange, the blue, the green, and the yellow vector is associated a score of 2,1,1,0, respectively. In this case, the orange vector is selected. Since the blue and the green vector lie inside the consensus set of the orange one, all the star subsets that are adopted to generate these three vectors are considered in the generation of the new $\boldsymbol{s}_{\mathrm{indx_{new}}}$.

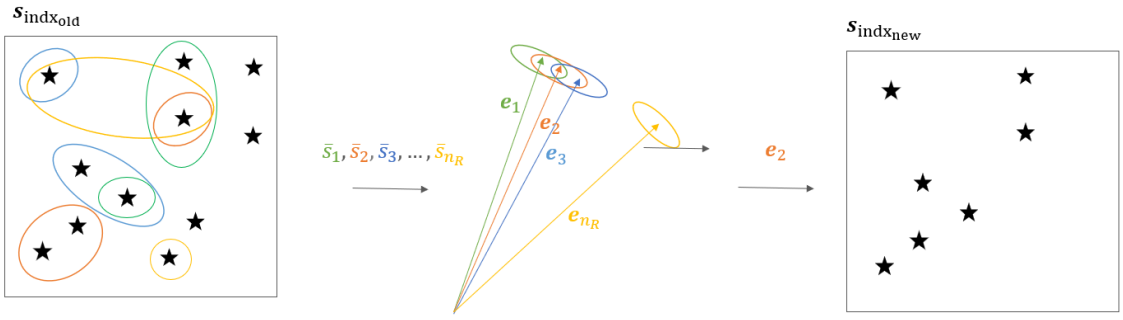

Figure 3: Graphical Representation of the RANSAC Algorithm

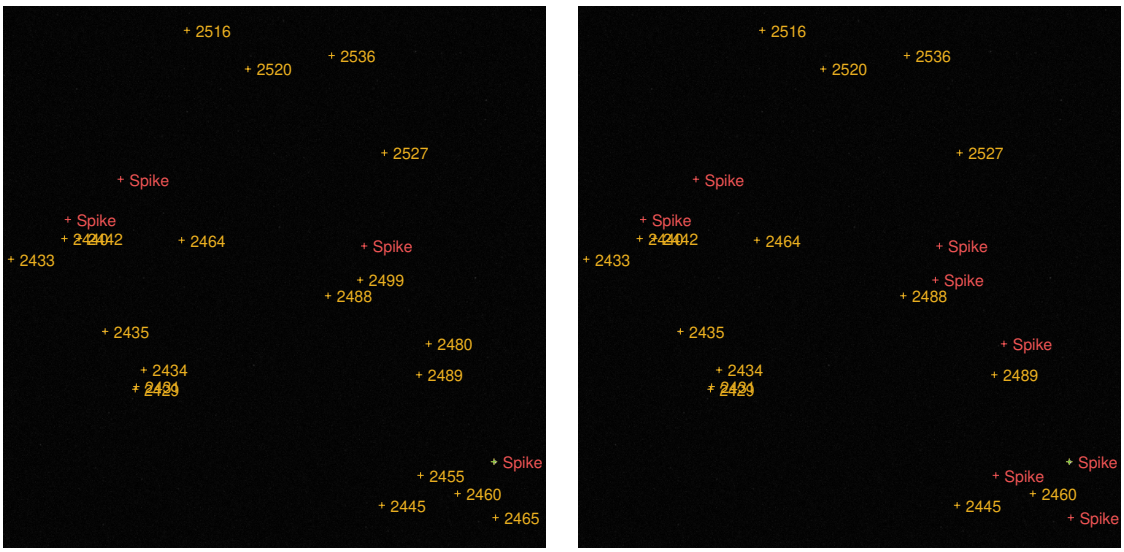

(a) Stars Pattern Before RANSAC

(b) Stars Pattern After RANSAC

Figure 4: Results before and after the application of the RANSAC algorithm

Attitude Determination Starting from the new $\boldsymbol{s}_{\mathrm{indx_{new}}}$, the updated matrices $[{}^{\mathcal{N}}s_{\mathrm{new}}]$ and $[{}^{\mathcal{C}}s_{\mathrm{new}}]$ can be found. Once a matching between directions in $\mathcal{C}$ and directions in $\mathcal{N}$ is performed, the rotation matrix $[A]$ can be computed by solving the Wahba's problem. The Wahba's problem solution

is here computed by the Singular Value Decomposistion (SVD) method:[21]

$$[B] = \sum_{i=1}^{n_{\mathrm{AR}}} {}^{\mathcal{C}}\boldsymbol{s}_i \, {}^{\mathcal{N}}\boldsymbol{s}_i^{\top} \tag{9}$$

where n_{AR} is the total number of identified stars in the image after the RANSAC procedure and ${}^{\mathcal{C}}\boldsymbol{s}_i$ and ${}^{\mathcal{N}}\boldsymbol{s}_i$ are the ith columns of $[{}^{\mathcal{C}}s_{\mathrm{new}}]$ and $[{}^{\mathcal{N}}s_{\mathrm{new}}]$, respectively. As the $[B]$ matrix is not orthonormal due to measurements errors, the closest orthonormal matrix $[A]$ can be computed by imposing the matrix eigenvalues. Thus:

$$[B] = [U][S][V]^{\top} \rightarrow [A] = [U][M][V]^{\top}; \tag{10}$$

where $[M]$ is used to impose a right-handed reference frame and it is defined as:

$$[M] = \begin{bmatrix} 1 & 0 & 0 \\ 0 & 1 & 0 \\ 0 & 0 & \det[U]\det[V] \end{bmatrix} \tag{11}$$

Planet Identification Procedure and LoS Extraction

Once the attitude matrix $[A]$ is determined, the planet identification is performed. Assuming to know the probe position with a $3\sigma_r$ uncertainty on each Cartesian component and the planet ephemerides, the expected planet position projection ${}^{\mathbb{C}}\boldsymbol{R}_{\mathrm{pl}_0}$ is computed. If the planet ${}^{\mathbb{C}}\boldsymbol{R}_{\mathrm{pl}_0}$ falls inside the image boundaries, its related planet position projection covariance matrix due to the spacecraft pose, i.e. position and orientation, uncertainty is computed. This provides an area, in the image, where the considered planet projection is expected to be found - with 3σ probability - according to spacecraft pose uncertainty. If one or more spikes are contained in the planet projection 3σ uncertainty ellipse, the spike closest to the expected planet position projection is labeled as the correct planet position projection. This is because the closest to the ellipse center is the more probable - statistically - to be the correct planet position projection.

Planet Position Projection Covariance Matrix The planet position projection covariance matrix $[P]$ due to the spacecraft pose uncertainty is computed as

$$[P] = [F][S][F]^{\top} \tag{12}$$

where $[F]$ is the Jacobian matrix of the mapping linking the planet projection ${}^{\mathbb{C}}\boldsymbol{R}_{\mathrm{pl}}$ with the spacecraft pose, and $[S]$ is the uncertainty covariance matrix of the probe pose. To evaluate $[F]$, the variation of ${}^{\mathbb{C}}\boldsymbol{R}_{\mathrm{pl}}$ with respect to the spacecraft pose has to be computed. To simplify the calculus, the quaternions are chosen to represent the probe attitude matrix:

$$\delta\, {}^{\mathbb{C}}\boldsymbol{R}_{\mathrm{pl}} = \left[\frac{\partial\, {}^{\mathbb{C}}\boldsymbol{R}_{\mathrm{pl}}}{\partial q_0}\right]\delta q_0 + \left[\frac{\partial\, {}^{\mathbb{C}}\boldsymbol{R}_{\mathrm{pl}}}{\partial \boldsymbol{q}_v}\right]\delta \boldsymbol{q}_v + \left[\frac{\partial\, {}^{\mathbb{C}}\boldsymbol{R}_{\mathrm{pl}}}{\partial \boldsymbol{r}}\right]\delta \boldsymbol{r} \tag{13}$$

$$\delta\, {}^{\mathbb{C}}\boldsymbol{R}_{\mathrm{pl}} = \underbrace{\left[\left[\frac{\partial\, {}^{\mathbb{C}}\boldsymbol{R}_{\mathrm{pl}}}{\partial q_0}\right] \quad \left[\frac{\partial\, {}^{\mathbb{C}}\boldsymbol{R}_{\mathrm{pl}}}{\partial \boldsymbol{q}_v}\right] \quad \left[\frac{\partial\, {}^{\mathbb{C}}\boldsymbol{R}_{\mathrm{pl}}}{\partial \boldsymbol{r}}\right]\right]}_{[F]} \begin{pmatrix} \delta q_0 \\ \delta \boldsymbol{q}_v \\ \delta \boldsymbol{r} \end{pmatrix} \tag{14}$$

The matrix $[F]$ has dimension 2×7 and, by computing the derivatives of Eq. 4 and 5, is defined as

$$[F] = \underbrace{\begin{bmatrix} \frac{1}{{}^{\mathbb{C}}R_{\mathrm{pl}_3}} & 0 & -\frac{{}^{\mathbb{C}}R_{\mathrm{pl}_1}}{{}^{\mathbb{C}}R^2_{\mathrm{pl}_3}} \\ 0 & \frac{1}{{}^{\mathbb{C}}R_{\mathrm{pl}_3}} & -\frac{{}^{\mathbb{C}}R_{\mathrm{pl}_2}}{{}^{\mathbb{C}}R^2_{\mathrm{pl}_3}} \end{bmatrix}}_{\text{Derivative of Eq. 5}} \underbrace{[K] \begin{bmatrix} \frac{\partial([A]\,{}^{\mathcal{N}}\boldsymbol{\rho})}{\partial q_0} & \frac{\partial([A]\,{}^{\mathcal{N}}\boldsymbol{\rho})}{\partial \boldsymbol{q}_v} & \frac{\partial([A]\,{}^{\mathcal{N}}\boldsymbol{\rho})}{\partial \boldsymbol{r}} \end{bmatrix}}_{\text{Derivative Eq. 4}} \tag{15}$$

where the partial derivatives of $\partial([A]\,{}^{\mathcal{N}}\boldsymbol{\rho})$ with respect to the spacecraft pose are

$$\frac{\partial([A]\,{}^{\mathcal{N}}\boldsymbol{\rho})}{\partial q_0} = 2q_0\,{}^{\mathcal{N}}\boldsymbol{\rho} \tag{16}$$

$$\frac{\partial([A]\,{}^{\mathcal{N}}\boldsymbol{\rho})}{\partial \boldsymbol{q}_v} = -2\,{}^{\mathcal{N}}\boldsymbol{\rho}\boldsymbol{q}_v^{\top} + 2\boldsymbol{q}_v^{\top}\,{}^{\mathcal{N}}\boldsymbol{\rho}[I] + 2\boldsymbol{q}_v\,{}^{\mathcal{N}}\boldsymbol{\rho} - 2[{}^{\mathcal{N}}\boldsymbol{\rho}]^{\wedge} \tag{17}$$

$$\frac{\partial([A]\,{}^{\mathcal{N}}\boldsymbol{\rho})}{\partial \boldsymbol{r}} = -[A][\mathbb{I}_3] \tag{18}$$

On the other hand, $[S]$ is a $[7 \times 7]$ matrix and it is defined as

$$[S] = \begin{bmatrix} \sigma^2_{q_0} & 0 & 0 \\ [\mathbb{0}_{3\times3}] & \sigma^2_{\boldsymbol{q}_v}[\mathbb{I}_3] & [\mathbb{0}_{3\times3}] \\ [\mathbb{0}_{3\times3}] & [\mathbb{0}_{3\times3}] & \sigma^2_r[\mathbb{I}_3] \end{bmatrix} \tag{19}$$

Since the uncertainty of the probe orientation is more clearly identified through the Euler's principal rotation theorem. Let us link the variations of the quaternions with the pointing error. The variation of the quaternions with respect to the principal angle θ and the principal axis $\boldsymbol{e}$ are

$$\delta q_0 = \frac{\partial q_0}{\partial \theta}\delta\theta + \frac{\partial q_0}{\partial \boldsymbol{e}}\delta\boldsymbol{e} \qquad\qquad \delta\boldsymbol{q}_v = \frac{\partial \boldsymbol{q}_v}{\partial \theta}\delta\theta + \frac{\partial \boldsymbol{q}_v}{\partial \boldsymbol{e}}\delta\boldsymbol{e} \tag{20}$$

By knowing that $\boldsymbol{q}_v = \boldsymbol{e}\sin(\phi/2)$ and $q_0 = \cos(\phi/2)$ and assuming that $\theta \ll 1$, the total derivatives are

$$\begin{pmatrix} \delta q_0 \\ \delta q_{v1} \\ \delta q_{v2} \\ \delta q_{v3} \end{pmatrix} = \begin{bmatrix} -\frac{\theta}{4} & 0 & 0 & 0 \\ \frac{e_1}{2} & \frac{\theta}{2} & 0 & 0 \\ \frac{e_2}{2} & \frac{\theta}{2} & 0 & 0 \\ \frac{e_3}{2} & \frac{\theta}{2} & 0 & 0 \end{bmatrix} \begin{pmatrix} \delta\theta \\ \delta e_1 \\ \delta e_2 \\ \delta e_3 \end{pmatrix} \tag{21}$$

Moreover, if $\theta \simeq 0$, the expression becomes

$$\begin{pmatrix} \delta q_0 \\ \delta q_{v1} \\ \delta q_{v2} \\ \delta q_{v3} \end{pmatrix} = \begin{bmatrix} 0 & 0 & 0 & 0 \\ \frac{e_1}{2} & 0 & 0 & 0 \\ \frac{e_2}{2} & 0 & 0 & 0 \\ \frac{e_3}{2} & 0 & 0 & 0 \end{bmatrix} \begin{pmatrix} \delta\theta \\ \delta e_1 \\ \delta e_2 \\ \delta e_3 \end{pmatrix} \tag{22}$$

$$\delta q_0 = 0 \qquad\qquad \delta\boldsymbol{q}_v = \frac{1}{2}\boldsymbol{e}\delta\theta \tag{23}$$

Thus, $[S]$ becomes:

$$[S] = \begin{bmatrix} 0 & 0 & 0 \\ [\mathbb{0}_{3\times3}] & \sigma^2_{\boldsymbol{q}_v}[\mathbb{I}_3] & [\mathbb{0}_{3\times3}] \\ [\mathbb{0}_{3\times3}] & [\mathbb{0}_{3\times3}] & \sigma^2_r[\mathbb{I}_3] \end{bmatrix} \tag{24}$$

Planet Position Uncertainty Ellipses Once the planet position projection covariance matrix is found, the associated uncertainty ellipse is generated.

Let λ_1 and λ_2 be the largest and smallest eigenvalues of $[P]$, respectively, and $\boldsymbol{v}_1$, $\boldsymbol{v}_2$ their related eigenvectors. Note that $[P] \in \mathbb{R}^{2\times 2}$. The characteristics of the 3-σ covariance ellipse are:

$$a = 3\sqrt{\lambda_1} \qquad b = 3\sqrt{\lambda_2} \qquad \psi = \arctan\left(\frac{\boldsymbol{v}_{\max_y}}{\boldsymbol{v}_{\max_x}}\right) \tag{25}$$

where a is the 3-σ covariance ellipse semimajor axis, b the 3-σ covariance ellipse semiminor axis, and ψ the 3-σ covariance ellipse orientation of the ellipse (angle of the largest eigenvector towards the x-axis).

The equation of the planet position uncertainty ellipse as a function of the angle θ is so derived

$$\begin{bmatrix} x \\ y \end{bmatrix} = \begin{bmatrix} a\cos\theta & b\sin\theta \end{bmatrix} \begin{bmatrix} \cos\psi & \sin\psi \\ -\sin\psi & \cos\psi \end{bmatrix} + {}^{\mathbb{C}}\boldsymbol{R}_{\mathrm{pl}_0} \tag{26}$$

Planet Identification and Line-of-Sight Extraction At this point, the spikes inside the uncertainty ellipses are identified. The closest spike to the guessed position of the planet is identified as the planet itself. If no spike is present inside the planet projection 3-σ covariance ellipse, the planet is considered too faint to be observed by the camera at that position. Once the planet position ${}^{\mathbb{C}}\boldsymbol{R}_{\mathrm{pl}}$ is identified in the image, it is backprojected on the 3D world to find the planet LoS to be provided to the navigation filter.

Discussion about the algorithm

Since the star identification procedure is not performed with deterministic algorithms, one or more stars may be wrongly identified for a given starfield. Moreover, to identify the stars, a 1D k-vector exploiting only the interstar angle is applied. Differently from the statistic pyramid star identification technique[18] where the four-star polygon structure can be associated with an almost certain star identification, in the 1D k-vector, several combination of stars pairs whose interstar angle lies between $[\cos(\theta_{\mathrm{obs}} + 2\epsilon), \cos(\theta_{\mathrm{obs}} - 2\epsilon)]$ are present. This leads to a possible stars misidentification. To bulk up the stars identification procedure and reach the performances of the pyramid star identification technique, the RANSAC algorithm is applied. It should increase the robustness of the IP pipeline on two sides. Firstly, by recognizing and removing the stars wrongly identified, it should enhance the confidence level of the attitude estimation. Secondly, by identifying as outliers those non-stellar objects, as planets, mistaken for stars, it should decrease the rate of failure of the IP pipeline due to the non-recognition of the planets in the image. This particular failure case (" Failure A") will be detailed in the following section, and it is verified when the planet uncertainty ellipse contains a star, but not a spike.
Moreover, the IP pipeline may not be able to complete the stars identification step and recognize a star pattern. This occurs when a high number of non-cataloged objects is present in the given image. In this work, the non-cataloged objects are the planets and the stars with an absolute magnitude greater than a set threshold value, which has been imposed to limit the computational burden related to the creation of the ground-computed on-board-stored catalog of stars' invariants. The IP pipeline can recognize when this scenario takes place and associates to it an invalidity flag.
For what concerns planet identification, it is possible that, even if a planet is in the Field-of-View (FoV) of the camera, it is too faint to be detected by the IP procedure. This happens because, in this work, no planets selection based on the apparent magnitude has been included. Yet, since the

planets exploited for the VBN are usually the brightest ones,[11] this scenario has not been identified as a failure of the pipeline. In the procedure, this scenario is verified when the planet uncertainty ellipse does not include either a star or a spike. Similarly, a planet may be on the margin of the camera detector, but its estimated expected planet position projection falls outside of it. In this case, the planet uncertainty ellipse can not be determined. Nevertheless, this scenario is not considered as a failing one because during VBN the planet is expected to be about at the center of the camera detector.
Moreover, the size of the planet uncertainty ellipse is proportional to the uncertainty of the spacecraft position σ_r. When σ_r increases, the ellipse increases as well and the expected planet position projection is far from the true one. This leads to a most likely planet misidentification. For instance, it can happen that:

- Even if the planet is not detected by the centroiding algorithm and so no spikes are associated with the planet, its uncertainty ellipse includes other non-recognized objects. Thus, the IP pipeline wrongly identifies the closest one to the expected planet position projection as the planet itself.
- Since the expected planet position projection is very far from the true one, it can generate a planet uncertainty ellipse in which the closest spike is not the one associated with the planet centroid.

To recognize and discard these scenarios where the IP pipeline performs wrong planet identification, a validity flag is set. When the distance between the expected planet position and the closest spikes is larger than 50 px, the algorithm is assumed to fail (Failure B).

SIMULATION

In this section, the performances of the IP procedure for the planet LoS extraction are shown. After having described the simulation setting in detail, a Monte Carlo simulation of 1000 scenarios is run. Moreover, for sake of clarity, the main steps of the IP pipeline are illustrated applied to a test case. Finally, the robustness of the algorithm is discussed.

Simulation Settings

Synthetic Images Generation The processed images are generated exploiting the sky-field simulator described in Reference 9, where only an improvement in the modeling of the variance of the total noise is performed. At this aim, the procedure proposed by[22] is adopted. Moreover, the characteristics of the camera assumed onboard are reported in Table 1.

Table 1: Optical camera setup

FoV [deg]	Image size [px]	f [mm]	F[1] [-]	T [ms]	$Q_e \times T_{lens}$[2]	SEA[3] [deg]	σ_d[4] [px]
20	1024×1024	40	2.2	400	0.49	20	0.9

[1] f-number
[2] quantum efficiency $\times$ lens transmission
[3] Solar Exclusion Angle
[4] defocus level

Star Identification Settings The threshold value of the absolute magnitude considered for the development of the onboard catalogs is 5.5 for computational reasons. If an image contains fainter stars, these are labeled as spikes.

For what concerns the RANSAC procedure, 20 samples are considered. Indeed, it is assumed that the proportion of outliers in each sample subset (with a dimension of 3) is at most 40%.[14] Whereas, the threshold value t is set to 20 arcsec according to the camera measurement noise ($t = 3\sigma_{\text{meas}}$).[14]

Planet Line-of-Sight Extraction Settings To compute the planet position projection covariance matrix $[P]$, the probe pose uncertainties σ_θ and σ_r (see Eq. 24) are defined. As a result of a statistical analysis, σ_θ is set equal to 40 arcsec. Instead, the probe position uncertainty is initially assumed to be equal to $\sigma_r = 10^5$ km. Then, a sensitivity analysis is performed to analyze the robustness of the algorithm with respect to the initial uncertainty of the probe position.

Monte Carlo Campaign

To assess the performances of the developed algorithm a Monte Carlo campaign is carried on. The IP pipeline for the planet LoS extraction is run for 1000 scenarios wherein each one at least one planet is present. In each scenario the position of the spacecraft is randomly selected inside a 3σ ellipsoid with axis $a = b = 2\text{AU}$ km and $c = 10^6$ km and centered in the origin of $\mathcal{N}$. Similarly, the orientation of the probe is assigned by randomly choosing α, δ, and ϕ in the 3σ intervals $[0, 2\pi]$, $[-0.6, 0.6]$, and $[0, 2\pi]$, respectively. The declination δ is chosen in a narrower interval as planets are distributed close to the ecliptic plane. At each iteration, the attitude determination and planets LoS direction errors are evaluated with respect to their exact values. In particular, the attitude determination error is represented by the angle between the principal axis directions relative to the computed attitude matrix $[A]$ and to the one associated with the true attitude matrix $[CN]$. On the other hand, the planet LoS direction error is described by the angle between the computed and the true planet LoS directions, evaluated considering the spacecraft true position. Note that the attitude determination error is embedded inside the planet LoS direction error.
Tables 2 and 3 report the 1-σ dispersion of the estimated attitude errors (σ_{Rot}) and the 1-σ dispersion of the planet LoS direction errors (σ_{LoS}), respectively. Moreover, their cumulative density functions are shown in Figure 5.

Table 2: Statistics of the attitude determination error

σ_{Rot} [arcsec]	$\leq \sigma_{\text{Rot}}$ [%]	$\leq 2\sigma_{\text{Rot}}$ [%]	$\leq 3\sigma_{\text{Rot}}$ [%]
10.46	86	96.77	99.08

Table 3: Statistics of the planet Line-of-Sight direction error

σ_{LoS} [arcsec]	$\leq \sigma_{\text{LoS}}$ [%]	$\leq 2\sigma_{\text{LoS}}$ [%]	$\leq 3\sigma_{\text{LoS}}$ [%]
9.98	89.36	95.77	98.33

The error obtained in the extraction of the planet LoS can be also described as the residual between the planet true and estimated position in the pixel reference frame. The 1σ standard deviation of the residuals along the x and y directions of the pixel reference frame are reported in Tables 4 and 5. Moreover, the histogram representing the 2D distribution of the residuals is shown in Figure 6 with

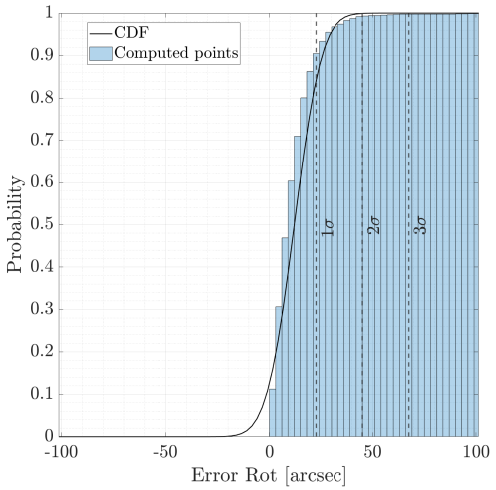

(a) Cumulative Distribution Function of the Attitude Error

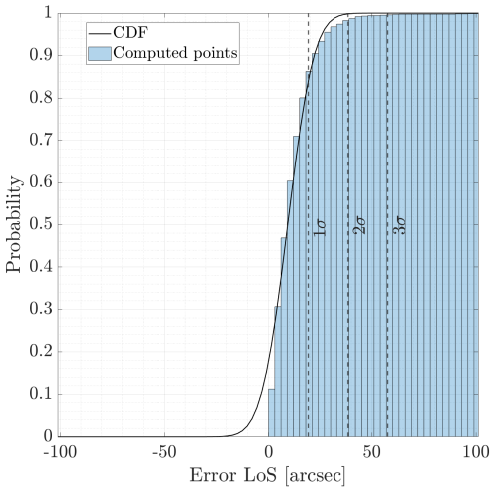

(b) Cumulative Distribution Function of the Planet LoS Error

Figure 5: Cumulative Distribution Function for 1000 scenarios and $\sigma_r = 10^5$ km

Table 4: Standard deviations and cumulative percentage of the planet position error along x

σ_{x} [px]	$\leq \sigma_{\mathrm{x}}$ [%]	$\leq 2\sigma_{\mathrm{x}}$ [%]	$\leq 3\sigma_{\mathrm{x}}$ [%]
0.14	85.59	95.07	98.29

Table 5: Standard deviations and cumulative percentage of the planet position error along y

σ_{y} [px]	$\leq \sigma_{\mathrm{y}}$ [%]	$\leq 2\sigma_{\mathrm{y}}$ [%]	$\leq 3\sigma_{\mathrm{y}}$ [%]
0.12	82.9	93.99	97.84

Table 6: Probe position and orientation for the test scenario

r [km]	α [rad]	δ [rad]	ϕ [rad]
$[-4.14; -5.43; 0.072] \cdot 10^7$	5.72	-0.04	0.05

1σ, 2σ, and 3σ bounds. Note that the distribution of the sample points is well represented by a Gaussian distribution.
Finally, the Monte Carlo simulation results in a percentage of failure of the IP pipeline of 0.2 %. See the subsection "Failure Cases" for the definition of different failures.

Test Case

The main steps that the IP pipeline performs to extract the planet LoS direction from the image are here graphically represented for one test scenario. In this scenario, the values of the probe position and orientation are reported in Table 6.
Before starting the procedure, the sky-field image relative to the assigned probe orientation is gen-

erated (see Figure 7).
Then, the stars identification procedure is performed. In Figure 8 the recognized star-pattern is shown; the marker $+$ represents the computed centroids of the stellar and not stellar objects. The bright objects that are not identified as stars by the k-vector and the RANSAC procedure are labeled as spikes. Once the star pattern is identified, the probe attitude matrix $[A]$ is computed. In this test

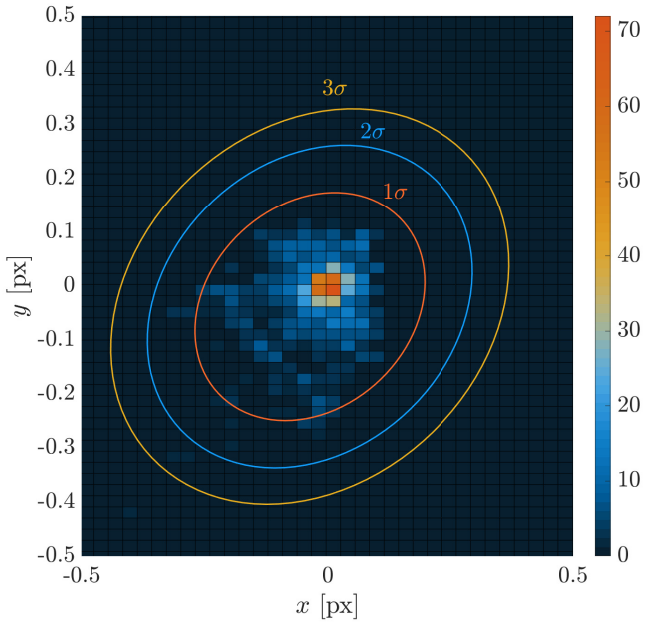

Figure 6: Gaussian distribution of the planet position projection errors with 1σ, 2σ, and 3σ bounds. The colorbar represents the number of samples that lie in each grid intervals.

Figure 7: The synthetic image is generated by the sky-field simulator[9]

scenario, the error performed in the determination of the probe orientation is 12.85 arcsec.

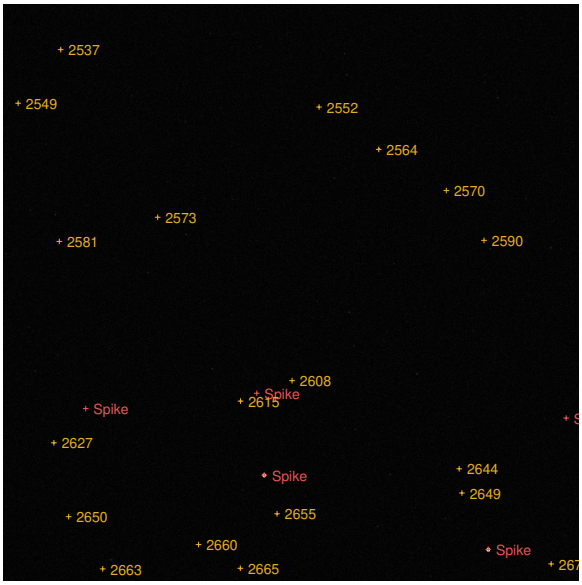

Figure 8: Stars and non-stellar objects are identified for the given starfield

At this point, by knowing $[A]$ and assuming to know the probe position with a 1σ uncertainty of 10^5 km, the expected position projection of all planets is computed. Only the planets whose position projection is contained inside the image boundaries are taken into account for the following steps. In Figure 9, the expected planets' position projections in the image are represented with a blue $*$. Afterward, the planet position projection covariance matrices $[P]$ associated with the planets in the image are determined. From this computation, the planet projection 3σ uncertainty ellipsoid, shown in yellow in Figure 9, are computed. Among the spikes contained in each ellipse, the closest to the expected planet position projection is identified as the planet itself as it is the most probable to be the expected planet. Once the planets are identified, their LoS direction is determined. In this case, the error performed in the estimation of the planets' LoS directions is 16.08 and 4.58 arcsec for Mercury and Jupiter, respectively.

Robustness

RANSAC The robustness of the IP pipeline is increased with the application of the RANSAC algorithm. To verify this, a Monte Carlo simulation without the application of the RANSAC procedure is performed. The settings adopted are equal to the one exploited in the section "Test Case". As expected, the percentage of failure increases in both the determination of the attitude of the spacecraft (8.16%) and in the extraction of the planet LoS (3.98%). The total percentage of failure is equal to 12.14%.

Failure Cases Despite the RANSAC algorithm increases greatly the robustness of the star identification procedure, failures in the determination of the probe attitude and in the planet LoS direction may happen. For what concerns the failures in the attitude determination, three situations can take place:

1. The star identification procedure can give as output a wrong star identification (one or more stars are wrongly identified)

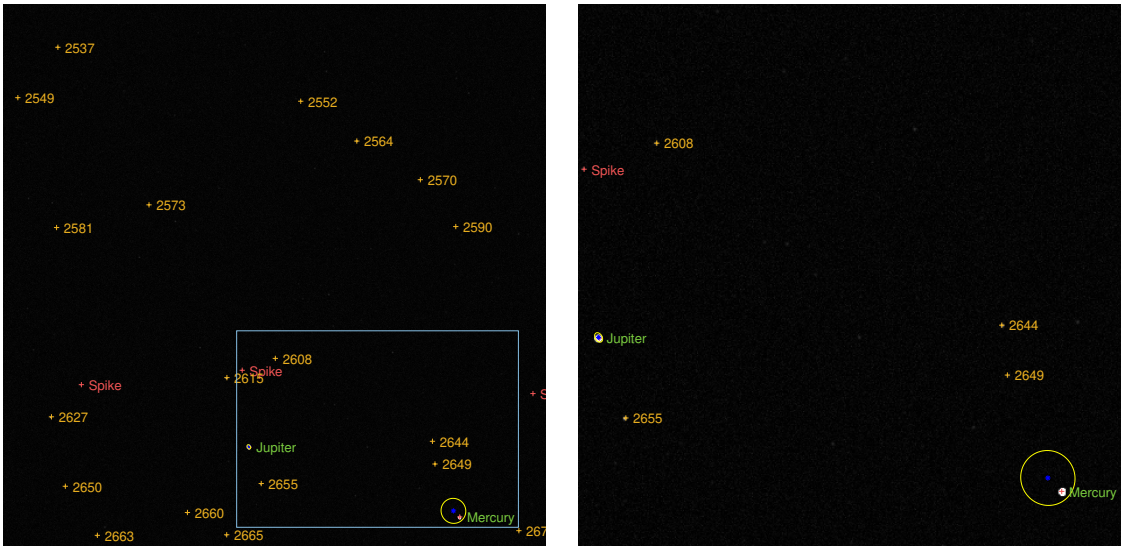

(a) Results of the planet identification procedure

(b) Close-up on the blue box

Figure 9: Planets are identified for the given starfield

2. The procedure does not converge to any identification at all
3. The number of stars in the field of view (FoV) is less than three.

The second and the third scenarios are not considered as actual operative failures since, when they happen, the algorithm can be simply run again slightly changing the camera view. When the second scenario happens, the failure is counted to assess the expounded failure statistics, and the Monte Carlo simulation moves directly to the next simulation. Moreover, even if the attitude is correctly determined, the procedure for the planet LoS extraction may fail. Two are the identified scenarios, both related to a spikes misidentification: A) No spikes inside the planet position uncertainty ellipse are detected (the planet is mistaken for a star), B) The closest spike has a distance from ${}^{\mathbb{C}}\boldsymbol{R}_{\mathrm{pl}_0}$ greater than 50 px. Besides the identified cases of failure, it is assumed that the algorithm fails whenever the LoS error is greater than 500 arcsec. This event is considered as a "not-recognized" failure (C). Figure 10 gives a representation of failures A, B, and C.

Sensitivity to position uncertainty A sensitivity analysis is performed to analyze the robustness of the IP pipeline to the increment of the uncertainty of the spacecraft position. In particular, two additional Monte Carlo simulations, over the one previously run, are performed by changing σ_r. Table 7 shows the results obtained when σ_r is set to 10^5, 10^6, and 10^7 km, respectively.

Table 7: Sensitivity analysis results as function of the position standard deviation error

σ_r [km]	σ_{Rot} [arcsec]	σ_{LoS} [arcsec]	% fail LoS	% fail attitude	% total fail
10^5	9.98	10.46	0.19	0.01	0.2
10^6	9.70	11.88	3.67	0.01	3.68
10^7	10.24	15	42.72	0.24	42.96

As expected, the standard deviations of the attitude determination and planet LoS direction errors

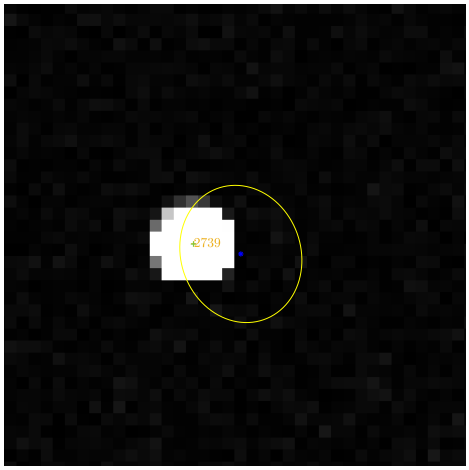

(a) Failure A: The planet is mistaken for a star.

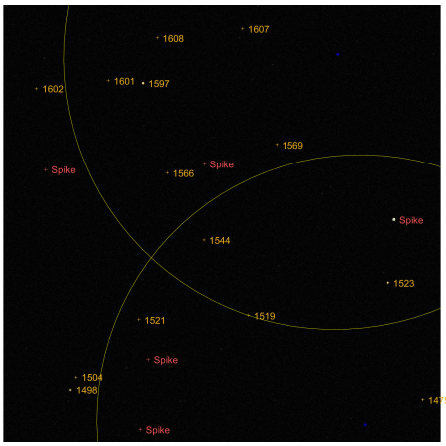

(b) Failure B: The distance between the closest spikes and the blue * is over 50 px.

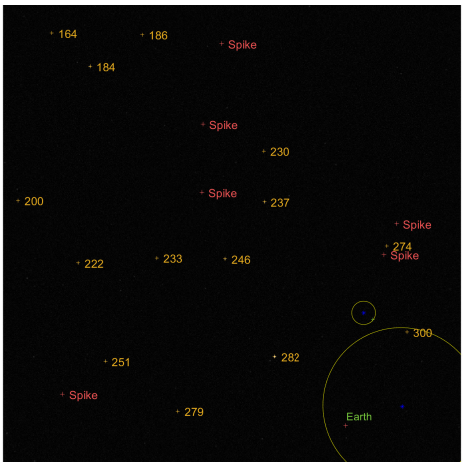

(c) Failure C: The only spike contained in the ellipse is wrongly identified as the planet.

Figure 10: Failures in the LoS extraction. The true projection of the position of the planet is identified with a green +, the expected one with a blue *.

do not have a significant increment with the increase of the uncertainty of the spacecraft position. This is because the latter only brings a variation of the shape and the position of the planet position uncertainty ellipse. If the spike that corresponds to the planet is inside that ellipse, the planet is determined, and the only errors that affect its determination are the ones associated with the centroids computation and attitude determination.

Instead, the percentage of failure of the IP pipeline increases significantly when the probe position uncertainty is set to 10^7 km. This is mainly due to a failure in the planet LoS extraction and takes place because the planet position uncertainty ellipses greatly increase in size, yielding to a wrong planet identification. On the other hand, since the star pattern identification does not depend on the knowledge of the position of the spacecraft, the rate of success in the attitude determination is

similar in all the scenarios. For sake of completeness, Table 8 reports the subdivision of the failure percentage of the planet LoS extraction with respect to the failure scenarios described in the section "Failure Cases".

Table 8: Failure percentage in the extraction of the planet LoS as function of the position standard deviation error

σ_r	A [%]	B [%]	C [%]	[%] Total
10^5	0.13	0	0.06	0.19
10^6	1.06	0.93	1.68	3.67
10^7	4.53	27.20	10.99	42.72

CONCLUSIONS

In this work, an innovative and robust image processing procedure for the extraction of the planets LoS has been proposed. The IP pipeline estimates the projection of the planet position with a 1σ accuracy lower than 0.2 pixels along both the x and the y axis and computes the attitude direction with a 1σ accuracy of about 10 arcseconds. Moreover, if the probe position is known with an accuracy equal or lower than 10^6 km, the procedure is proved to be robust with a rate of total failure below the 4%, which agrees with the result of the pyramid star identification technique.[18] This robustness is provided by both the application of the RANSAC algorithm and the computation of the planet position projection covariance matrix. The former detects the misidentified stars, whereas, the latter identifies and delimits the region in which the projection of the planet position can be found.
In this analysis, the IP pipeline is fed by synthetic images in which the camera noise is added. Whereas, future analysis will test the performances of the IP pipeline during hardware-in-the-loop simulations. In this context, a camera will acquire a starfield image, rendered on a high-resolution screen, and will give the associated matrix of digital counts to the IP algorithm.

ACKNOWLEDGMENTS

This research is part of EXTREMA, a project that has received funding from the European Research Council (ERC) under the European Union's Horizon 2020 research and innovation programme (Grant Agreement No. 864697).

REFERENCES

[1] T. Villela, C. Costa, A. Brandão, F. Bueno, and R. Leonardi, "Towards the Thousandth CubeSat: A Statistical Overview," *International Journal of Aerospace Engineering*, Vol. 2019, 01 2019, 10.1155/2019/5063145.

[2] S. M. Lichten, D. S. Abraham, B. Arroyo, S. W. Asmar, J. Bell, and C. D. Edwards, "Allocation of Deep Space Network Ground System Tracking and Communications Assets During the 2020-2021 Timeframe of the "Mars Armada"," *2018 SpaceOps Conference*, 2018, 10.2514/6.2018-2502.

[3] M. Quadrelli, L. J. Wood, J. E. Riedel, M. McHenry, M. Aung, L. Cangahuala, R. Volpe, P. Beauchamp, and J. A. Cutts, "Guidance, Navigation, and Control Technology Assessment for Future Planetary Science Missions," *Journal of Guidance Control and Dynamics*, Vol. 38, 2015, pp. 1165–1186.

[4] R. Karimi and D. Mortari, "Interplanetary Autonomous Navigation Using Visible Planets," *Journal of Guidance, Control, and Dynamics*, Vol. 38, 04 2015, pp. 1–6, 10.2514/1.G000575.

[5] G. D. Domenico, E. Andreis, A. C. Morelli, G. Merisio, V. Franzese, C. Giordano, A. Morselli, P. Panicucci, F. Ferrari, and F. Topputo, "Toward Self-Driving Interplanetary CubeSats: The ERC-funded project EXTREMA," *72nd International Astronautical Congress*, 10 2021.

[6] M. D. Shuster *et al.*, "A survey of attitude representations," *Navigation*, Vol. 8, No. 9, 1993, pp. 439–517.

[7] R. Hartley and A. Zisserman, *Camera Models*, ch. 3, pp. 117–120. Cambridge University Press 2000, 2004.

[8] M. A. C. Perryman, L. Lindegren, J. Kovalevsky, E. Hog, U. Bastian, P. L. Bernacca, M. Creze, F. Donati, M. Grenon, M. Grewing, F. van Leeuwen, H. van der Marel, F. Mignard, C. A. Murray, R. S. Le Poole, H. Schrijver, C. Turon, F. Arenou, M. Froeschle, and C. S. Petersen, "The Hipparcos Catalogue.," *Astronomy and Astrophysics*, Vol. 500, jul 1997, pp. 501–504.

[9] S. A. Bella, E. Andreis, V. Franzese, P.Panicucci, and F. Topputo, "Line-of-Sight Extraction Algorithm for Deep-Space Autonomous Navigation," *2021 AAS/AIAA Astrodynamics Specialist Conference*, 08 2021.

[10] V. Franzese, F. Topputo, F. Ankersen, and R. Walker, "Deep-Space Optical Navigation for M-ARGO Mission," *The Journal of the Astronautical Sciences*, Vol. 68, No. 4, 2021, pp. 1034–1055.

[11] E. Andreis, V. Franzese, and F. Topputo, "An Overview of Autonomous Optical Navigation for Deep-Space CubeSats," *72nd International Astronautical Congress*, 10 2021.

[12] D. Mortari, "Search-Less Algorithm for Star Pattern Recognition," *Journal of the Astronautical Sciences*, Vol. 45, 04 1997, 10.1007/BF03546375.

[13] B. Spratling and D. Mortari, "A Survey on Star Identification Algorithms," *Algorithms*, Vol. 2, 03 2009, 10.3390/a2010093.

[14] R. Hartley and A. Zisserman, *Estimation – 2D Projective Transformations*, ch. 3, pp. 117–120. Cambridge University Press 2000, 2004.

[15] L. Kazemi, J. Enright, and T. Dzamba, "Improving star tracker centroiding performance in dynamic imaging conditions," *2015 IEEE Aerospace Conference*, 2015, pp. 1–8, DOI: 10.1109/AERO.2015.7119226.

[16] X. Jiang, S. Li, L. Gu, J. Sun, and D. Xiao, "Optical Image Generation and High-precision Line-of-Sight Extraction for Mars Approach Navigation," *Journal of Navigation*, Vol. 72, No. 1, 2019, p. 229–252, DOI: 10.1017/S0373463318000450.

[17] A. Vyas, M. B. Roopashree, B. R. Prasad, and A. Vyas, "Performance of Centroiding Algorithms at Low Light Level Conditions in Adaptive Optics," *2009 International Conference on Advances in Recent Technologies in Communication and Computing*, 2009, pp. 366–369, DOI: 10.1109/ARTCom.2009.30.

[18] D. Mortari, M. A. Samaan, C. Bruccoleri, and J. L. Junkins, "The pyramid star identification technique," *Navigation*, Vol. 51, No. 3, 2004, pp. 171–183.

[19] B. B. Spratling and D. Mortari, "A survey on star identification algorithms," *Algorithms*, Vol. 2, No. 1, 2009, pp. 93–107.

[20] M. A. Fischler and R. C. Bolles, "Random sample consensus: a paradigm for model fitting with applications to image analysis and automated cartography," *Communications of the ACM*, Vol. 24, No. 6, 1981, pp. 381–395.

[21] F. L. Markley, "Attitude determination using vector observations and the singular value decomposition," *Journal of the Astronautical Sciences*, Vol. 36, No. 3, 1988, pp. 245–258.

[22] J. A. Christian, *Optical navigation for a spacecraft in a planetary system*. PhD thesis, 2010.